Shaping of arm configuration space by prescription of non-Euclidean metrics with applications to human motor control

Armin Biess*

Bernstein Center for Computational Neuroscience and Max-Planck-Institute for Dynamics and Self-Organization, 37077 Göttingen, Germany

(Received 21 July 2012; revised manuscript received 17 October 2012; published 31 January 2013)

The study of the kinematic and dynamic features of human arm movements provides insights into the computational strategies underlying human motor control. In this paper a differential geometric approach to movement control is taken by endowing arm configuration space with different non-Euclidean metric structures to study the predictions of the generalized minimum-jerk (MJ) model in the resulting Riemannian manifold for different types of human arm movements. For each metric space the solution of the generalized MJ model is given by reparametrized geodesic paths. This geodesic model is applied to a variety of motor tasks ranging from three-dimensional unconstrained movements of a four degree of freedom arm between pointlike targets to constrained movements where the hand location is confined to a surface (e.g., a sphere) or a curve (e.g., an ellipse). For the latter speed-curvature relations are derived depending on the boundary conditions imposed (periodic or nonperiodic) and the compatibility with the empirical one-third power law is shown. Based on these theoretical studies and recent experimental findings, I argue that geodesics may be an emergent property of the motor system and that the sensorimotor system may shape arm configuration space by learning metric structures through sensorimotor feedback.

DOI: 10.1103/PhysRevE.87.012729 PACS number(s): 87.19.rs, 45.10.Na, 02.40.Ky, 87.19.lr

I. INTRODUCTION

One of the classical models of computational human motor control theory is the minimum-jerk (MJ) model that describes the kinematic features of arm movements between pointlike targets in a horizontal plane [1]. The MJ model is formulated in terms of Cartesian hand position coordinates $\boldsymbol{x}$ and is derived from a kinematic cost functional that minimizes the squared time derivative of the hand acceleration or jerk integrated over the total movement duration T, i.e.,

$$\delta C_{\mathrm{MJ}} = 0\,,\; C_{\mathrm{MJ}} = \int_0^T \left\langle \frac{d^3\boldsymbol{x}(t)}{dt^3}, \frac{d^3\boldsymbol{x}(t)}{dt^3} \right\rangle_I dt\,, \qquad (1)$$

where $\langle\,,\rangle_I$ denotes the inner product with respect to the Euclidean metric $I = \mathrm{diag}(1,1)$. The solution of the MJ variational problem (1) subject to the two-point boundary conditions

$$\begin{aligned} \boldsymbol{x}(0) &= \boldsymbol{x}_0, \quad & \boldsymbol{x}(T) &= \boldsymbol{x}_f \\ \dot{\boldsymbol{x}}(0) &= 0, \quad & \dot{\boldsymbol{x}}(T) &= 0 \\ \ddot{\boldsymbol{x}}(0) &= 0, \quad & \ddot{\boldsymbol{x}}(T) &= 0 \end{aligned} \qquad (2)$$

is given by

$$\boldsymbol{x}(t) = \boldsymbol{x}_0 + (\boldsymbol{x}_f - \boldsymbol{x}_0)(6\tau^5 - 15\tau^4 + 10\tau^3)\,, \qquad (3)$$

where $\tau = t/T$ denotes normalized time and $\boldsymbol{x}_0, \boldsymbol{x}_f$ are the initial and final target locations, respectively. Thus the MJ solution results in straight hand paths and bell-shaped hand-speed profiles, which are in excellent agreement with experimental data. Although this model was developed more than three decades ago and new modeling approaches have been proposed [2–6], it is still widely used in basic research of human motor control [7], robotics [8,9], and rehabilitation research [10–12]. The success of this model lies, besides its predictive power, in its simplicity and analytical tractability. However, the MJ model is limited in its application to the description of motor tasks in Euclidean space, which is not necessarily the geometric structure underlying human movements. Interestingly, more than a century ago Mach and Poincaré [13,14] pointed out the fundamental differences between sensory and motor spaces to Euclidean space with regard to continuity, dimensionality, spatial extension, homogeneity, and isotropy. Different geometrical structures have been applied to model various sensorimotor spaces, such as perceptual, tactile, and haptic spaces. Perceptual space has been investigated most extensively, and different non-Euclidean geometric structures have been proposed, ranging from Riemannian manifolds with varying curvature [15,16] to nonmetric spaces with affine or projective geometry [17,18]. Fasse and colleagues [19] have argued that some aspects of human perceptual-motor behavior may not admit a metric description, and Flash and Handzel have modeled human tracing movements using affine geometry [20]. A theory of movement timing based on geometrical invariance and affine geometry has been proposed in [21].

In recent studies [22,23] a reinterpretation of the MJ model in form of a geodesic model in Euclidean space has been provided and a generalization to arbitrary Riemannian arm configuration manifolds has been formulated. The resulting generalized MJ model (or geodesic model) can be applied to arbitrary Riemannian manifolds and, as I will show, is applicable to a wider class of motor tasks. Apart from the extension of scope, a Riemannian formulation has the advantage of being inherently coordinate independent. In models of human motor control one has to distinguish between external coordinates or frames of references that the investigator is choosing to describe a motor action (e.g., an arm movement) and the internal coordinates of a putative neural representation of this event in the central nervous system (CNS). Although some progress has been made to identify the neural correlates of movements [24–27], very little is

*armin@nld.ds.mpg.de

known about possible coordinate system(s) used by the CNS. A coordinate-free description of models of human motor control provides therefore an unbiased approach that is independent of the arbitrary choice of coordinates by the investigator.

That the choice of coordinates can be problematic in models of human motor control has been recently pointed out by Sternad and colleagues [28] in the context of motor variability and the uncontrolled manifold (UCM) concept [29]. The UCM method aims to identify control variables based on the analysis of motor performance variability in tasks with redundancy. It relies on the analysis of covariance matrix anisotropy in execution space (e.g., joint angular space) as evidence for the coordinates of movement control as well as on orthogonality to distinguish task-relevant from task-irrelevant directions. However, anisotropy and orthogonality of a covariance matrix depend significantly on the investigator's arbitrary choice of external coordinates, and thus, no consistent inferences about neural movement control can be drawn from such an analysis. In contrast, in a Riemannian description movement variability can be assessed independently from the choice of coordinates.

Of similar importance to movement control is the identification of movement invariants, i.e., of movement variables that do not change under general coordinate transformations. Invariants provide useful signatures of the computational model at hand and their identification is at the core of Riemannian geometry.

The paper is organized as follows: In Sec. II I recapitulate the main properties of the geodesic model and list the main features of the model when applied to a configuration manifold that is endowed with the kinetic energy metric. In Sec. III arm configuration space is shaped by constructing metric tensors from hand and elbow displacements in task space. In contrast to the kinetic energy metric, which is associated with the dynamics of the movement, these metrics are derived from task space and may thus be related to visual space. Interestingly, when applying the geodesic model to these preshaped metric spaces, a large variety of motor tasks can be described ranging from unconstrained point-to-point movements in three-dimensional space to constrained movements where the end effector is following a predefined surface or a curve. For the latter speed-curvature relations are derived depending on the boundary conditions imposed (periodic and nonperiodic) and the relation to the empirical one-third power law is analyzed.

II. METHODS

A. Arm configuration space and coordinate systems

The arm is modeled as a linkage of rigid bodies. The arm's configuration space Q can be regarded as an n-dimensional torus $T^n = S^1 \times \cdots \times S^1$, i.e., as the n-fold direct product of the circle S^1. In the present article I consider types of movements for which the degrees of freedom (DOFs) at the wrist and finger joints can be ignored (for example, in an experimental setting the wrist can be fixated and the forearm, hand, and fingers can be treated as one rigid body). Accordingly, an arm configuration can be described by means of four coordinates ($n = 4$), for example, in terms of four joint angles $\boldsymbol{q} = (\theta,\eta,\zeta,\phi)^T$. The first three angles determine the rotation around an ideally spherical shoulder joint (elevation θ, azimuth η, torsion ζ), whereas the rotation around the elbow joint is given by the flexion angle (ϕ).

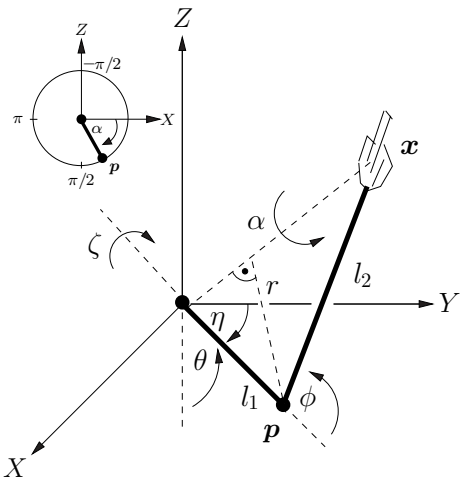

FIG. 1. An arm configuration can be defined by different sets of coordinates, for example, by four joint angular coordinates $\boldsymbol{q} = (\theta,\eta,\zeta,\phi)^T$. Another possible set of generalized coordinates consists of the center of mass of the hand location $\boldsymbol{x}$ and the swivel angle α around the shoulder-hand axis, i.e., $\boldsymbol{q}' = (x,y,z,\alpha)^T$. The shoulder joint is fixated and located at the origin of the XYZ coordinate system. The vector $\boldsymbol{p}$ denotes the elbow location, $d = |\boldsymbol{x}|$ is the shoulder-hand distance, r is the radial distance to the elbow location from the shoulder-hand axis, l_1 denotes the upper arm length, and l_2 is the distance from the elbow joint to the center of mass of the hand (forearm and hand are modeled as one rigid body). The insert shows the definition of the swivel angle α.

Another possible set of four generalized coordinates is defined by $\boldsymbol{q}' = (x,y,z,\alpha)^T$, which consists of the hand coordinates $\boldsymbol{x}$ augmented by the swivel angle α that describes the rotation of the upper arm and forearm triangle around the shoulder-hand axis (Fig. 1). Note that there exists a one-to-one map between these coordinate sets. The coordinate differentials are related via the transformation matrix $\Lambda = (\Lambda^\mu_\nu)$:

$$dq'^\mu = \Lambda^\mu_\nu(q)dq^\nu \quad \text{with} \quad \Lambda^\mu_\nu = \frac{\partial q'^\mu}{\partial q^\nu}, \tag{4}$$

where the summation convention has been used, implying a summation over the same lower and upper Greek indices from 1 to 4. Explicit expressions for the one-to-one map between the two sets of coordinates are provided in Appendix A. The transformation matrix Λ is given in [23]. Yet another natural coordinate system can be generated by replacing the Cartesian hand coordinates (x,y,z) by cylindrical coordinates (ρ,φ,z), where the body-axis coincides with the z axis. This new set of coordinates $\boldsymbol{q}'' = (\rho,\varphi,z,\alpha)$ may be well adapted to the body-centered notions of far-near (ρ), left-right (φ), and up-down (z). Obviously, there are many coordinates that are equally well suited to define an arm configuration. One advantage of the application of Riemannian geometry to models of human motor control is the inherent independence from this arbitrary choice of coordinates.

B. Geodesic model

In this section the geodesic model is recapitulated by considering the one-parameter family of optimization problems

given by the mean-squared derivative (MSD) cost functionals in Riemannian space:

$$\delta S_n = 0\,,\; S_n = \int_0^T \left\langle \frac{D^n\gamma(t)}{dt^n}, \frac{D^n\gamma(t)}{dt^n} \right\rangle dt\,, \tag{5}$$

subject to the boundary conditions

$$\begin{aligned} \gamma(0) &= a\,, & \gamma(T) &= b \\ \tfrac{D\gamma(0)}{dt} &= 0\,, & \tfrac{D\gamma(T)}{dt} &= 0 \\ &\vdots & &\vdots \\ \frac{D^{n-1}\gamma(0)}{dt^{n-1}} &= 0\,, & \frac{D^{n-1}\gamma(T)}{dt^{n-1}} &= 0. \end{aligned} \tag{6}$$

Note that the functional (5) defines for $n = 3$ the Riemannian generalization of the classical MJ functional (1). The inner product $\langle\,,\rangle$ in (5) is defined with respect to an arbitrary Riemannian metric g. The operator $\frac{D}{dt}$ denotes the covariant derivative in the direction of the trajectory $\gamma(t)$, i.e., $\frac{D}{dt} := \nabla_{\dot\gamma(t)}$, and ∇ is the Levi-Civita connection, which is the symmetric connection compatible with the metric. The k-fold covariant derivative along the trajectory is denoted by $\frac{D^k}{dt^k}$,$k = 1,2,\ldots$.

The Euler-Lagrange equations for the variational problems (5) follow from the application of the calculus of variation on manifolds [30,31]. For $n > 0$ one obtains [32–34]

$$\frac{D^{2n}\gamma(t)}{dt^{2n}} + \sum_{i=0}^{n-2}(-1)^i R\left(\frac{D^{2n-2-i}\gamma(t)}{dt^{2n-2-i}}, \frac{D^{i+1}\gamma(t)}{dt^{i+1}}\right)\frac{d\gamma(t)}{dt} = 0\,, \tag{7}$$

where R is the Riemann curvature tensor defined by $R(\boldsymbol{X},\boldsymbol{Y})\boldsymbol{Z} = [\nabla_{\boldsymbol{X}},\nabla_{\boldsymbol{Y}}]\boldsymbol{Z} - \nabla_{[\boldsymbol{X},\boldsymbol{Y}]}\boldsymbol{Z}$ for arbitrary vector fields $\boldsymbol{X},\boldsymbol{Y},\boldsymbol{Z}$ and $[\,,\,]$ denotes the commutator [35]. The solution of the Euler-Lagrange equation (7) subject to the boundary conditions is given by reparametrized geodesic paths $\gamma(t) = \gamma(\sigma(t))$ between two points a and b in the Riemannian arm configuration manifold [23]. The spatial and temporal aspects of the movement decouple: the spatial properties (path, posture) are determined by the geodesic equation

$$\nabla_{\gamma'(\sigma)}\gamma'(\sigma) = 0, \quad n = 1,2,\ldots \tag{8}$$

subject to the boundary conditions

$$\gamma^\mu(0) = a, \qquad \gamma^\mu(\Sigma) = b\,, \tag{9}$$

where a prime denotes differentiation with respect to arc length. The temporal properties (speed) follow by reparametrization of arc length into time and are governed by

$$\frac{d^{2n}\sigma(t)}{dt^{2n}} = 0, \quad n = 1,2\ldots\,, \tag{10}$$

subject to the $2n$-boundary conditions

$$\begin{aligned} \sigma(0) &= 0, & \sigma(T) &= \Sigma\,, \\ \dot\sigma(0) &= 0, & \dot\sigma(T) &= 0\,, \\ &\vdots & &\vdots, \\ \frac{d^{n-1}\sigma(0)}{dt^{n-1}} &= 0, & \frac{d^{n-1}\sigma(T)}{dt^{n-1}} &= 0, \end{aligned} \tag{11}$$

where Σ is the total length of the geodesic path. Equation (10), subject to (11), can be solved analytically in terms of the generalized hypergeometric function ${}_2F_1$ [36]:

$$\sigma_n(\tau) = \Sigma\frac{(2n-1)!\,\tau^n}{(n-1)!^2\,n}\,{}_2F_1(n;1-n;n+1;\tau)\,, \tag{12}$$

where $\tau = t/T$ denotes normalized time. In particular, it follows for $n = 1,2,3$:

$$\sigma_n(\tau) = \begin{cases} \Sigma\tau\,, & n = 1\,, \\ \Sigma(-2\tau^3 + 3\tau^2)\,, & n = 2\,, \\ \Sigma(6\tau^5 - 15\tau^4 + 10\tau^3)\,, & n = 3\,. \end{cases} \tag{13}$$

Note that the optimal solution predicts the same geodesic path $\gamma(\sigma)$ for different values of n, but results according to (10) in different parametrizations along the geodesic path. For example, the original MJ model ($n = 3$) is obtained for Euclidean task space $\mathcal{M} = (\mathbb{R}^2, I)$, where $I = \mathrm{diag}(1,1)$ is the Euclidean metric. The equations (5), (8), and (10) take then the form

$$\delta S_3 = 0\,,\; S_3 = \int_0^T \left\langle \frac{d^3\boldsymbol{x}(t)}{dt^3}, \frac{d^3\boldsymbol{x}(t)}{dt^3} \right\rangle_I dt\,, \tag{14}$$

$$\frac{d^2\boldsymbol{x}(s)}{ds^2} = 0 \quad \text{and} \quad \frac{d^6 s(t)}{dt^6} = 0\,, \tag{15}$$

where s is the Euclidean arc length. Combining the solutions of (15) subject to the boundary conditions (9) and (11), respectively, leads to the well-known MJ solution (3).

Instead of two-point boundary conditions (11), periodic boundary conditions can be imposed:

$$\begin{aligned} \sigma(0) &= 0\,,\; \sigma(T) = \Sigma\,, \\ \dot\sigma(0) &= \dot\sigma(T)\,, \\ &\vdots \\ \frac{d^{2n-2}\sigma(0)}{dt^{2n-2}} &= \frac{d^{2n-2}\sigma(T)}{dt^{2n-2}}\,. \end{aligned} \tag{16}$$

Using a Fourier "ansatz" (see Appendix B) the optimal solution for all orders of n is

$$\sigma_n(\tau) = \Sigma\tau, \quad n = 1,2,\ldots\,, \tag{17}$$

It follows that for periodic movements normalized Riemannian arc length, $\tilde\sigma = \sigma/\Sigma$, is equal to normalized time, and thus time can be measured directly in terms of arc-length.

Movements along geodesic paths lead to constants of motion, which are given by [23,33,34]

$$I_n = \frac{(-1)^{n-1}}{2}\left(\frac{d^n\sigma}{dt^n}\right)^2 + \sum_{j=1}^{n-1}(-1)^{(j-1)}\frac{d^{2n-j}\sigma}{dt^{2n-j}}\frac{d^j\sigma}{dt^j}\,. \tag{18}$$

In particular, for $n = 1,2,3$ one derives

$$I_n = \begin{cases} \frac{1}{2}\dot\sigma^2\,, & n = 1\,, \\ \dddot\sigma\dot\sigma - \frac{1}{2}\ddot\sigma^2\,, & n = 2\,, \\ \sigma^{(5)}\dot\sigma - \sigma^{(4)}\ddot\sigma + \frac{1}{2}\dddot\sigma^2\,, & n = 3\,. \end{cases} \tag{19}$$

Note that these constants of motion are invariants because σ is a scalar. Invariants are useful signatures of a computational model that can be easily subject to experimental tests. For example, the original MJ model leads to $I_3 = (30\sqrt{2}S)^2/T^6$, where S is the total Euclidean distance to the target.

Another class of invariants may be derived from symmetries of the metric tensor in the form of Killing vector fields. For further details the readers are referred to [23,35]. Finally, the functional (5) scales under a change of amplitude, $\tilde{\gamma}(t) = \omega\gamma(t)$, and time, $\tilde{t} = \beta t$, according to $\tilde{S}_n = \omega^2\beta^{1-2n}S_n$, and thus the optimal solution is invariant under these transformations. It is important to emphasize that the results provided in this section hold for any Riemannian manifold $\mathcal{M} = (T^4, g)$.

1. Kinetic-energy metric

One natural metric follows from the dynamic equation of motion of the arm, which can be written in covariant form as [23,37]

$$M_{\mu\nu}A^{\nu} = \tau_{\mu}\,, \tag{20}$$

where A^{μ} denotes the covariant acceleration and τ_{μ} the joint torques. The manipulator inertia matrix (kinetic energy metric) $M_{\mu\nu}$ defines a metric and is derived from the kinetic energy K according to

$$M_{\mu\nu}(q) = \frac{\partial^2 K(q,\dot{q})}{\partial\dot{q}^{\mu}\partial\dot{q}^{\nu}}\,. \tag{21}$$

The corresponding line element is given by

$$d\sigma^2 = M_{\mu\nu}(q)dq^{\mu}dq^{\nu} \tag{22}$$

and the kinetic energy can be expressed as

$$K = \tfrac{1}{2}\dot{\sigma}^2\,. \tag{23}$$

In previous studies [22,23] the predictions of the geodesic model using this metric have been analyzed in detail and the following properties could be derived.

First, geodesic paths with respect to the kinetic energy metric correspond to least-effort paths, suggesting that the kinetic energy metric may be associated with the proprioceptive feedback stream. Second, in *this* metric space the MJ model is equivalent to the minimum torque-change model [2], i.e., one derives

$$\int_0^T \left\langle \frac{D\boldsymbol{A}(t)}{dt}, \frac{D\boldsymbol{A}(t)}{dt} \right\rangle dt = \int_0^T \left\langle \frac{D\boldsymbol{\tau}(t)}{dt}, \frac{D\boldsymbol{\tau}(t)}{dt} \right\rangle dt, \tag{24}$$

where the inner product $\langle\,,\rangle$ is taken with respect to the metric (21). It is important to remark that these models are fundamentally different when expressed in Euclidean space. Third, the minimum peak value of kinetic energy model by Soechting and co-workers [3] is compatible with the geodesic model, as I will show next. This model has been proposed to resolve the redundancy in a point-to-point movement task, in which the final arm posture (defined by four DOFs) is not specified by the three spatial coordinates of the given final target location. According to Soechting's model the final arm posture is determined by the trajectory that adopts the minimal-peak value of kinetic energy.

To reanalyze this model within the Riemannian framework, boundary conditions of the form

$$\boldsymbol{q}(0) = \boldsymbol{q}_0\,, \quad \boldsymbol{x}(\Sigma) = \boldsymbol{x}_f \tag{25}$$

are imposed. The vectors $\boldsymbol{q}_0$ and $\boldsymbol{x}_f$ denote the predefined initial arm posture and the final target location, respectively. In the four-dimensional configuration manifold the final arm postures are described by a one-dimensional manifold corresponding to all accessible arm postures compatible with the final target location. Biomechanical joint range models can be used to select the accessible final arm postures (for details see [22]). There is thus a one-parameter family of geodesic paths γ_{α} connecting the initial arm posture with the possible final ones. The parameter α is chosen to be the swivel angle at the final target location (Fig. 1). The peak value of the kinetic energy $\hat{K}_{\alpha}$ associated with each path γ_{α} can be derived from (23) using (13) for $n = 3$. Assuming that the total movement time is independent of the path, i.e., $T_{\alpha} = T$ for all α (isochrony principle), one finds

$$\hat{K}_{\alpha} = \frac{1}{2}\left(\frac{15}{8T}\right)^2 \Sigma_{\alpha}^2\,, \tag{26}$$

where Σ_{α} is the total length of the geodesic path γ_{α}. Minimizing over the total length of geodesic paths results in a path with a minimal-peak kinetic energy, implying that the minimum peak value of kinetic energy model is an outcome of the geodesic model.

2. Jacobi metric

Another metric that is related to the dynamics is the Jacobi metric. If the torques can be derived from a potential function $V(q)$, the dynamic equation of motion (20) takes the form

$$M_{\mu\nu}A^{\nu} = -V_{,\mu}\,, \tag{27}$$

where a comma indicates a partial derivative, i.e., $V_{,\mu} = \frac{\partial V}{\partial q^{\mu}}$. For such a system the total energy E is conserved, i.e., $E = K + V = \frac{1}{2}M_{\mu\nu}\dot{q}^{\mu}\dot{q}^{\nu} + V = \text{const}$. The Jacobi metric is conformally related to the kinetic energy metric $M_{\mu\nu}$ and is defined by

$$\tilde{M}_{\mu\nu} = 2[E - V(q)]M_{\mu\nu}, \tag{28}$$

with line element $d\tilde{\sigma}^2 = \tilde{M}_{\mu\nu}dq^{\mu}dq^{\nu}$. It can then be shown that the dynamic equation of motion (27) is equivalent to the geodesic equation with respect to the Jacobi metric, i.e.,

$$\frac{d^2q^{\mu}}{d\tilde{\sigma}^2} + \tilde{\Gamma}^{\mu}_{\nu\lambda}\frac{dq^{\nu}}{d\tilde{\sigma}}\frac{dq^{\lambda}}{d\tilde{\sigma}} = 0\,. \tag{29}$$

This result poses the question whether it can be regarded as the optimal solution to the MSD costs in Riemannian space equipped with the Jacobi metric. Clearly, this is generally not the case because the dynamics depends on the specific choice of the potential function and is thus not necessarily compatible with the result (10) derived from the MSD costs.

III. RESULTS

A. Metrics related to displacements in task space

The kinetic energy and Jacobi metric are two examples of metrics in the arm configuration manifold that are related to the arm dynamics. The most general form of the metric in the four-dimensional arm configuration manifold is given by

$$d\sigma^2 = g_{\mu\nu}(x)dx^{\mu}dx^{\nu} \quad (\mu,\nu = 1,\ldots,4)\,. \tag{30}$$

Assuming that there exists a metric tensor $g_{\mu\nu}(x)$ in the configuration manifold, it would be a difficult task to determine

the ten components from empirical movement data. A more heuristic approach is therefore chosen in this paper, where Riemannian metrics are constructed "by hand," for example, by combining elbow and hand displacements in task space. I argue that these metrics can be associated with the visual input streams since their effect is to straighten the hand path. The imposed metric structure shapes arm configuration space and in combination with the geodesic model generates a specific motor behavior.

The first distance measure that I consider is defined in the coordinates $q'^{\mu} = (x,y,z,\alpha)$ and is given by the metric tensor

$$N'_{\mu\nu}(q') = \mathrm{diag}[1,1,1,\kappa r^2(d)]\,. \tag{31}$$

Here, r denotes the radius to the elbow location around the shoulder-hand axis and $d = |\boldsymbol{x}|$ is the shoulder-hand distance (Fig. 1). κ ($\kappa > 0$) defines a positive relative weight factor. The corresponding line element has the form

$$\begin{aligned} d\sigma^2 &= N'_{\mu\nu}(q')dq'^{\mu}dq'^{\nu} = dx^2 + dy^2 + dz^2 + \kappa r^2\alpha^2\,, \\ &= ds^2 + \kappa r^2 d\alpha^2\,, \end{aligned} \tag{32}$$

where $ds^2 = dx^2 + dy^2 + dz^2$ is the Euclidean line element associated with the end-effector location $\boldsymbol{x}$. The circular elbow radius r depends on the distance d according to ($0 < d < l_1 + l_2$),

$$r(d) = \frac{1}{2d}\sqrt{4d^2l_1^2 - \left(l_1^2 - l_2^2 + d^2\right)^2}\,. \tag{33}$$

The motivation for this choice of metric is twofold. First, the line element (32) measures the distance covered by the hand increased by the distance of the elbow position around the rotational DOF α. Note that the circular elbow radius r decreases with increasing shoulder-hand distance d. The underlying assumption here is that the motor system intends to minimize displacements of the whole arm system. Second, the line element (32) reduces for constant swivel angle α to the Euclidean line element $d\sigma^2 = ds^2$, in particular, for movement in a horizontal plane it is $d\alpha = dz = 0$ and $ds^2 = dx^2 + dy^2$. The geodesic model applied to this Riemannian space thus includes the classical MJ model as a special case. The metric tensor (31) can be expressed in the coordinates $q^{\mu} = (\theta,\eta,\zeta,\phi)$ by the following transformation:

$$N_{\mu\nu}(q) = \Lambda^{\lambda}_{\mu}(q)N'_{\lambda\rho}(q)\Lambda^{\rho}_{\nu}(q)\,, \tag{34}$$

where $N'_{\lambda\rho}(q)$ has the same form as (31) with $d = l_1^2 + l_2^2 + 2l_1l_2\cos\phi$. Although the components of $N_{\mu\nu}(q)$ involve large algebraic expressions, they can be easily determined using symbolic software packages (e.g., Mathematica, Maple).

I study next the predictions of the generalized MJ model ($n = 3$) for point-to-point arm movements in the Riemannian manifold equipped with the metric (31).

Spatial movement properties. The path predictions follow by solving numerically the geodesic equations (8) (for details see [23]). Since the metric tensor has a simpler form in the coordinates q'^{μ}, it is useful to perform all calculations in this coordinate system. The geodesic equation takes the form

$$\frac{d^2q'^{\mu}}{d\sigma^2} + \Gamma'^{\mu}_{\nu\lambda}\frac{dq'^{\nu}}{d\sigma}\frac{dq'^{\lambda}}{d\sigma} = 0\,, \tag{35}$$

with nonvanishing Christoffel symbols of the second kind:

$$\Gamma'^{i}_{44} = -\kappa\frac{\left[\left(l_1^2 - l_2^2\right)^2 - d^4\right]}{4d^4}q'^{i}\,, \tag{36}$$

$$\Gamma'^{4}_{4i} = \frac{\left[\left(l_1^2 - l_2^2\right)^2 - d^4\right]}{d^2\left[l_1^4 + \left(d^2 - l_2^2\right)^2 - 2l_1^2\left(l_2^2 + d^2\right)\right]}q'^{i}, \tag{37}$$

and $i = 1,2,3$. Boundary conditions of the form (25) are imposed:

$$\boldsymbol{q}'(0) = \boldsymbol{q}'_0\,, \quad q'^{i}(\Sigma) = \boldsymbol{x}_f^{(i)}\,, \quad (i = 1,2,3)\,, \tag{38}$$

where $\boldsymbol{x}_f^{(i)}$ denotes the i component of the given final target location $\boldsymbol{x}_f$. That is, the final arm configuration is not yet specified.

Temporal movement properties. The temporal properties of the movement are determined by (10) and (11), leading to

$$\dot{\sigma} = \frac{15}{8}\frac{\Sigma}{T}[4\tau(1-\tau)]^2 \tag{39}$$

Spatiotemporal movement properties. The movement trajectory follows by reparametrization of the path, i.e., $q'^{\mu}(t) = q'^{\mu}(\sigma(t))$. The velocity vector of the movement is obtained from the chain rule according to

$$\frac{dq'^{\mu}(t)}{dt} = \dot{\sigma}\frac{dq'^{\mu}(\sigma)}{d\sigma}\Big|\sigma = \sigma(t)\,, \tag{40}$$

where $\frac{dq'^{\mu}(\sigma)}{d\sigma}$ is the tangent vector of the geodesic path in configuration space. The hand speed v follows directly from the line element (32), giving

$$v = \sqrt{\dot{\sigma}^2 - \kappa r^2\dot{\alpha}^2}, \tag{41}$$

where $v = \frac{ds}{dt}$. For constant swivel angle α equation (32) leads to $d\sigma = ds$ and the geodesic model becomes identical with the classical MJ model (1).

Invariances. The Killing vectors of the metric $N'_{\mu\nu}(q')$ are determined next. Since the metric tensor is rotationally invariant and does not depend on the swivel angle α, the following four Killing vectors can be identified:

$$\boldsymbol{\xi}_{(1)} = y\frac{\partial}{\partial z} - z\frac{\partial}{\partial y}\,, \tag{42}$$

$$\boldsymbol{\xi}_{(2)} = z\frac{\partial}{\partial x} - x\frac{\partial}{\partial z}\,, \tag{43}$$

$$\boldsymbol{\xi}_{(3)} = x\frac{\partial}{\partial y} - y\frac{\partial}{\partial x}\,, \tag{44}$$

$$\boldsymbol{\xi}_{(4)} = \frac{\partial}{\partial\alpha}\,. \tag{45}$$

Note that each Killing vector induces a movement invariant $J_{(k)} = N'_{\mu\nu}(q')\xi^{\mu}_{(k)}t^{\nu}$ along geodesic motion with tangent vector $t^{\mu} = \frac{dq'^{\mu}}{d\sigma}$. These movement invariants can be subject to experimental tests for model validation.

Simulations. Simulation results for the generalized MJ model ($n = 3$) with free-end-point conditions are shown in Figs. 2(a)–2(c). Figure 2(a) shows the hand paths to nine

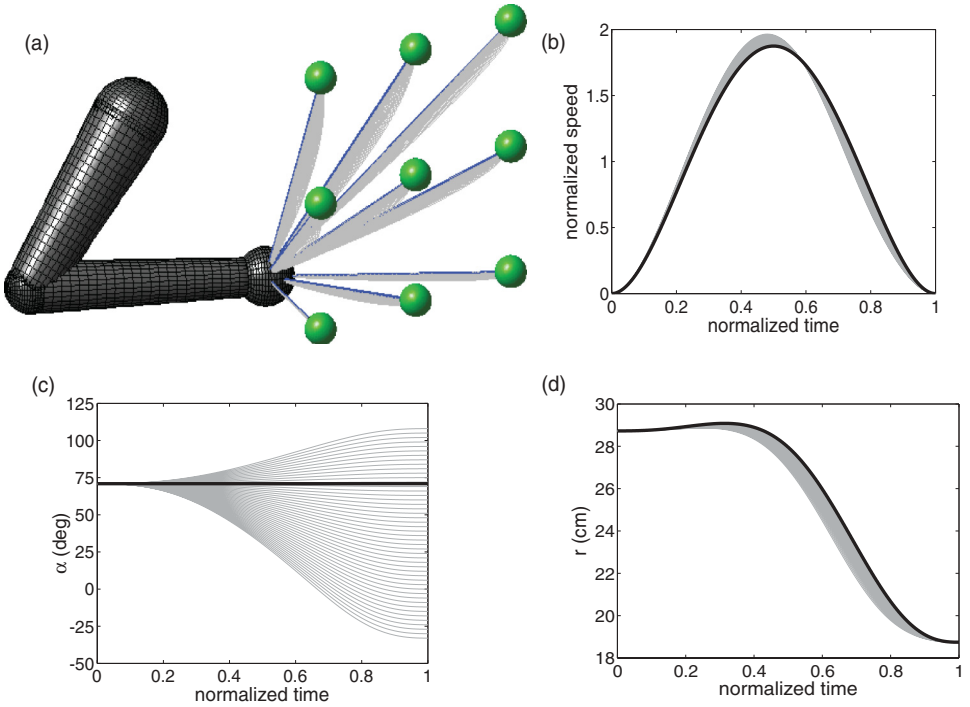

FIG. 2. (Color online) Predictions of the geodesic model with task space metric (32) for movements between pointlike targets in a fronto-parallel plane. (a) Predictions of hand paths to pointlike targets arranged in a fronto-parallel plane. The hand paths (shown in gray) vary and lead to different final arm postures at the target locations. The straight hand paths (shown in blue) correspond to the shortest geodesics connecting the initial with the final targets. (b) Normalized speed profiles, $\tilde{v} = v/(S/T)$, for movements to the upper-middle target. S is the Euclidean arc-length of the hand path and T denotes the total movement time. (c) Swivel angle trajectories for movements to the upper-middle target. (d) Radial distance to the elbow location from the shoulder-hand axis for movements to the upper-middle target. The profiles shown in black correspond to the movement along the shortest geodesic to the upper-middle target. Simulation parameters are provided in Table I.

targets arranged in a fronto-parallel plane. Note that the hand paths to each final target are derived from geodesic paths in the Riemannian manifold $\mathcal{M} = (T^4, N'_{\mu\nu})$ between a given initial arm configuration and all the accessible final arm configurations compatible with the given target location. It follows from the line element (32) that the shortest geodesic path out of the one-parameter family of geodesic paths is the straight hand path with constant swivel angle throughout the movement. Note that the minimal geodesic path ($\alpha = const$) leads with (41) to a MJ speed profile along the path, whereas trajectories with varying swivel angle ($\alpha \neq const$) deviate slightly from the MJ prediction. Figures 2(b) and 2(c) show the speed profiles and swivel angles, respectively, to one target (upper middle). For comparison, the same graphs using the kinetic energy metric are presented in Fig. 3. Clearly, the shaping of the configuration manifold by different metric structures induces different motor behavior. Another feature can be observed from these simulations: Without adding a stochastic element, the hand paths show variability in task space due to redundancy at the end point. Since each hand path corresponds to a different geodesic path in the configuration manifold, hand-path variability can be described by the concept of geodesic deviation.

Similar metrics to the one in (31) can be constructed. For example, consider a metric defined by the line element

$$d\sigma^2 = \boldsymbol{dx}^2 + \kappa \boldsymbol{dp}^2 = ds^2 + \kappa \boldsymbol{dp}^2 , \qquad (46)$$

which is composed out of the squared hand and elbow displacements. Note that the elbow location $\boldsymbol{p}$ depends on the end-effector location $\boldsymbol{x}$ and the swivel angle α (see Appendix A). In contrast to (34), this line element also measures translational displacements of the elbow position. Thus, the geodesic model results in movements with minimal changes of elbow and wrist displacements. Yet another metric can be defined by the line element

$$d\sigma^2 = \boldsymbol{dx}^2 + \kappa \boldsymbol{dx}_{\text{CM}}^2 = ds^2 + \kappa \boldsymbol{dx}_{\text{CM}}^2 , \qquad (47)$$

where $\boldsymbol{x}_{\text{CM}}$ is the center of mass of the whole arm system. The center of mass is determined under the assumption that the limbs are of cylindrical shape with constant mass density. For this simple arm model an analytical expression for the center of mass can be derived (Appendix C). One finds

$$\boldsymbol{x}_{\text{CM}} = \frac{1}{2(m_1 + m_2)}[(m_1 + m_2)\boldsymbol{p} + m_2 \boldsymbol{x}], \qquad (48)$$

where m_1 and m_2 are the masses of the upper arm and the forearm + hand, respectively. Thus the center of mass lies in the plane spanned by the upper and forearm.

B. Linear combinations of metrics

New metrics can be constructed by linear combinations of metrics since the sum of two Riemannian metrics defines another Riemannian metric. For example, to model the combined effect of visual and proprioceptive feedback, a new

TABLE I. Simulation parameters.

Parameter		Value	Reference
Arm model			
	Upper arm length l_1	0.30 m	Adjusted
	Forearm + hand l_2	0.375 m	Adjusted
	Upper arm mass m_1	2.52 kg	Adjusted
	Forearm mass m_2	2.07 kg	Adjusted
	Distance to center of mass, upper arm a_1	0.142 m	Adjusted
	Distance to center of mass, forearm a_2	0.244 m	Adjusted
	Moment of inertia I_1	0.351 kg m^2	[23]
	Moment of inertia I_2	0.019 kg m^2	[23]
	Moment of inertia I_3	0.269 kg m^2	[23]
	Moment of inertia I_4	0.024 kg m^2	[23]
	Moment of inertia I_5	0.152 kg m^2	[23]
Point-to-point movements—task space metric			
	Initial arm posture	$\boldsymbol{q}_0' = [-0.15$ m, 0.15 m, -0.25 m, 1.24 rad]	Adjusted
	Weight parameter	$\kappa = 1$	Adjusted
	Total movement time	$T = 1$ s	Adjusted
	Target locations	$\boldsymbol{X} = [-0.35\ \ 0.5\ \ 0.2; -0.15\ \ 0.5\ \ 0.2; 0.05\ \ 0.5\ \ 0.2; -0.35\ \ 0.5\ \ 0; -0.15\ \ 0.5\ \ 0; 0.05\ \ 0.5\ \ 0; -0.35\ \ 0.5\ \ -0.2; -0.15\ \ 0.5\ \ -0.2; 0.05\ \ 0.5\ \ -0.2]$ m.	Adjusted
Point-to-point movements—kinetic energy metric			
	Metric tensor	$M_{\mu\nu}$	[23]
	Initial arm posture	$\boldsymbol{q}_0 = [0.63, -1.80, 2.78, 2.15]$ rad $\triangleq \boldsymbol{q}_0'$	Adjusted
	Weight parameter	$\kappa = 1$	Adjusted
	Total movement time	$T = 1$ s	Adjusted
	Target locations	as above	
Point-to-point movements on a sphere			
	Initial position	$[\vartheta_0, \varphi_0] = [\pi/6, -\pi/3]$	Adjusted
	Final position	$[\vartheta_f, \varphi_f] = [2\pi/3, -\pi/3]$	Adjusted
	Weight parameter	$\kappa = 10$	Adjusted
	Center location of sphere	$\boldsymbol{m} = [0, 0.6, -0.3]$ m	Adjusted
	Radius of sphere	$R = 0.4$ m	Adjusted
	Total movement time	$T = 1$ s	Adjusted
Tracing movements of planar contours			
	Total tracing time	$T = 3$ s	Adjusted
	Perimeter of contours	$P = 0.67$ m	Adjusted
Ellipse	Major axis	$a = 0.13$ m	Adjusted
	Minor axis	$b = 0.08$ m	Adjusted
Cloverleaf	Size	$a = 0.069$ m	Adjusted
Limaçon	Size	$a = 0.1$ m	Adjusted
Lemniscate	Size	$a = 0.051$ m	Adjusted
	Shape	$b = 2.6$	Adjusted
	Line-element parameter	$\mu = 0.1$	Adjusted

metric can be defined by

$$G_{\mu\nu}(q) = (1 - w)M_{\mu\nu}(q) + wN_{\mu\nu}(q)\,, \tag{49}$$

where w is a weighting factor, $M_{\mu\nu}$ is the kinetic energy metric, and $N_{\mu\nu}$ is the metric in task space (34) expressed in the coordinates $\{q^\mu\}$. The setting $w = 1$ results in pure visual feedback, whereas $w = 0$ corresponds to proprioceptive feedback only. Generally, through the linear combination of metrics different distance measures can be integrated into a single description and the resulting cost functional can be decomposed into a sum of functionals:

$$S_n = \sum_i w_i \int_0^T \left\langle \frac{D^n\gamma(t)}{dt^n}, \frac{D^n\gamma(t)}{dt^n} \right\rangle_{g_i}, \tag{50}$$

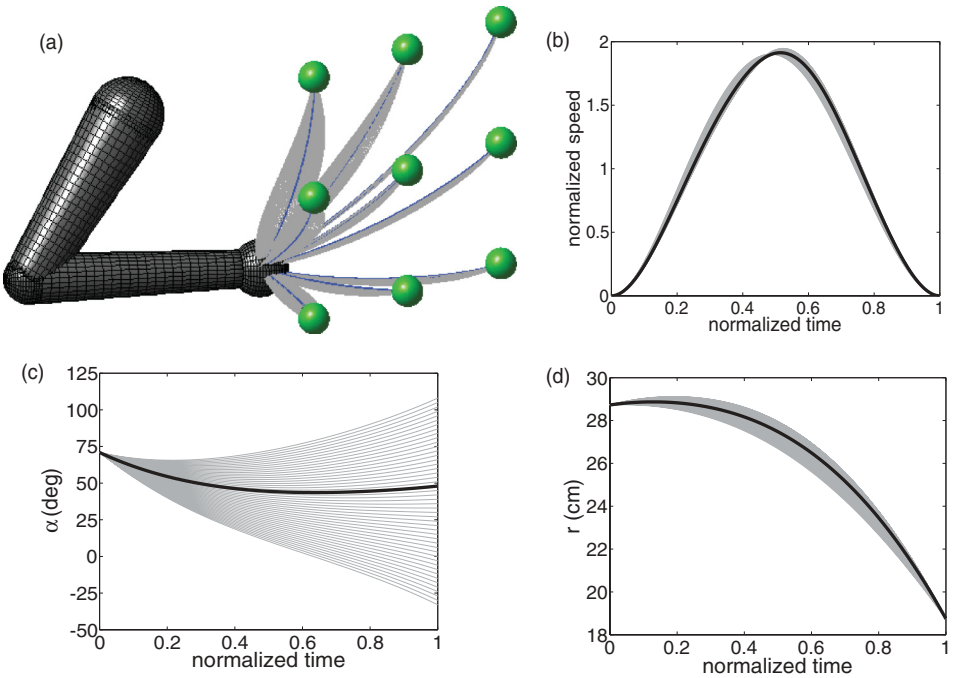

FIG. 3. (Color online) Predictions of the geodesic model with kinetic energy metric for movements between pointlike targets in a fronto-parallel plane. Same settings as in Fig. 2. The components of the metric tensor are provided in [23]. Predictions of hand paths to the same point-like targets as in Fig. 1. (a) The shortest geodesics connecting the initial with the final targets are shown in blue. Normalized speed profiles (b), swivel angles (c), and elbow radial distances (d) to the upper-middle target. The profiles shown in black correspond to the movement along the shortest geodesic to the upper-middle target. Simulation parameters are provided in Table I.

where the metric in arm configuration space is $g = \sum_i w_i g_i$ with weights $w_i \geqslant 0$.

C. Constrained arm movements along surfaces

In this section arm movements are studied for which the end effector is constrained to move along a predefined surface. Consider a parametric surface in three-dimensional space given by $\boldsymbol{x} = \boldsymbol{x}(u,v)$ with parameters u and v. The induced metric on the surface due to the embedding into Euclidean space (pullback metric) is

$$ds^2 = E(u,v)du^2 + 2F(u,v)dudv + G(u,v)dv^2, \quad (51)$$

where

$$E(u,v) = \frac{\partial \boldsymbol{x}}{\partial u} \cdot \frac{\partial \boldsymbol{x}}{\partial u}, \quad (52)$$

$$F(u,v) = \frac{\partial \boldsymbol{x}}{\partial u} \cdot \frac{\partial \boldsymbol{x}}{\partial v}, \quad (53)$$

$$G(u,v) = \frac{\partial \boldsymbol{x}}{\partial v} \cdot \frac{\partial \boldsymbol{x}}{\partial v}. \quad (54)$$

Metrics of arm configuration space can be thus obtained by replacing the Euclidean line element in (32) with (51), resulting in

$$d\sigma^2 = E(u,v)du^2 + 2F(u,v)dudv + G(u,v)dv^2 + \kappa r^2(u,v)d\alpha^2. \quad (55)$$

For simplicity, I will consider in the following arm movements where the hand is constrained to a spherical surface with radius R. Such movements may arise, for example, by holding a handle that is fixated at one end by a spherical joint. The origin of the coordinate system is set into the shoulder joint. The spherical surface is then given by $\boldsymbol{x}(\vartheta,\varphi) - \boldsymbol{m} = (R\sin\vartheta\cos\varphi, R\sin\vartheta\sin\varphi, R\cos\vartheta)$, where $\boldsymbol{m}$ is the center of the sphere. The line element (55) transforms to

$$d\sigma^2 = R^2(d\vartheta^2 + \sin^2\vartheta d\varphi^2) + \kappa r^2(\vartheta,\varphi)d\alpha^2, \quad (56)$$

where the shoulder-hand distance is given by $r(\vartheta,\varphi) = |\boldsymbol{x}(\vartheta,\varphi) + \boldsymbol{m}|$. The metric (56) adopts one Killing vector field

$$\boldsymbol{\xi} = \frac{\partial}{\partial \alpha}. \quad (57)$$

It is useful to distinguish the two cases of constant and changing swivel angle α.

Case 1: $\alpha = const$. In this case the swivel angle in (56) is kept fixed and only the end-effector movement on the sphere is of interest. The metric reduces then to the well-known line element on the sphere S^2,

$$d\sigma^2 \equiv ds^2 = R^2(d\vartheta^2 + \sin^2\vartheta d\varphi^2), \quad (58)$$

which adopts three Killing vector fields. The spatial prediction of the MSD cost functionals in this Riemannian space are determined by geodesic paths, i.e., great circles, for all orders of n. The end-effector speed is governed by

$$\frac{d^{2n}s(t)}{dt^{2n}} = 0 \quad (59)$$

with boundary conditions (11).

This Riemannian formulation is compared next to the standard modeling approach in Euclidean space by applying the original MJ model (1) to the sphere. More generally, I consider the one-parameter family of MSD cost functionals in Euclidean space for $n = 1,2,3$:

$$C_n = \int_0^T \left\langle \frac{d^n\boldsymbol{x}(t)}{dt^n}, \frac{d^n\boldsymbol{x}(t)}{dt^n} \right\rangle_I dt \quad (60)$$

subject to the constraint

$$\boldsymbol{x}^2(t) = R^2, \quad (61)$$

and boundary conditions

$$\begin{aligned} \boldsymbol{x}(0) &= \boldsymbol{x}_0, \quad & \boldsymbol{x}(T) &= \boldsymbol{x}_f \\ \dot{\boldsymbol{x}}(0) &= 0, \quad & \dot{\boldsymbol{x}}(T) &= 0 \\ &\vdots \quad & &\vdots, \\ \frac{d^{n-1}\boldsymbol{x}(0)}{dt^{n-1}} &= 0, \quad & \frac{d^{n-1}\boldsymbol{x}(T)}{dt^{n-1}} &= 0 \end{aligned} \tag{62}$$

where $I = \mathrm{diag}(1,1,1)$ is the Euclidean metric in three-dimensional space. Note that the difference between the Riemannian and Euclidean formulation is the embedding of the sphere in Euclidean space, which is not required in the former.

The standard method of Lagrange multipliers applied to (60) and (61) leads to the following dynamic equation of motion:

$$n = 1 : \ddot{\boldsymbol{x}} = \frac{\dot{\boldsymbol{x}}^2}{R}\boldsymbol{n}\,, \tag{63}$$

$$n = 2 : \boldsymbol{x}^{(4)} = \frac{3\ddot{\boldsymbol{x}}^2 + 4\dot{\boldsymbol{x}}\dddot{\boldsymbol{x}}}{R}\boldsymbol{n}\,, \tag{64}$$

$$n = 3 : \boldsymbol{x}^{(6)} = \frac{10\dddot{\boldsymbol{x}}^2 + 15\ddot{\boldsymbol{x}}\boldsymbol{x}^{(4)} + 6\dot{\boldsymbol{x}}\boldsymbol{x}^{(5)}}{R}\boldsymbol{n}\,, \tag{65}$$

with the normal vector $\boldsymbol{n} = -\boldsymbol{x}/R$.

Solutions to these equations can be found by first expressing the movement trajectory as $\boldsymbol{x}(t) = \boldsymbol{x}(s(t))$ and deriving higher-order time derivatives using Frenet's formulas. This leads to

$$\dot{\boldsymbol{x}} = \dot{s}\boldsymbol{t}\,, \tag{66}$$

$$\ddot{\boldsymbol{x}} = \ddot{s}\boldsymbol{t} + k\dot{s}^2\boldsymbol{n}\,, \tag{67}$$

$$\dddot{\boldsymbol{x}} = (\dddot{s} - k^2\dot{s}^3)\boldsymbol{t} + (k'\dot{s}^3 + 3k\dot{s}\ddot{s})\boldsymbol{n} + (\dot{s}^3 k\tau)\boldsymbol{b} \tag{68}$$

$$\ldots\,.$$

The vectors $\{\boldsymbol{t},\boldsymbol{n},\boldsymbol{b}\}$ are the tangent, normal, and binormal vectors of the path, respectively, and define an orthonormal moving frame along the trajectory. k denotes the curvature of the path and τ its torsion. Comparison of the expressions (63)–(65) with these formulas, leads to conditions for k,τ, and s. Using this method the solution of (63)–(65) for $n = 1,2,3$ is given by great circles, i.e.,

$$k = \frac{1}{R}\,,\ \tau = 0\,, \tag{69}$$

and temporal profiles $s(t)$ described by the following ordinary differential equations (ODEs):

$$\begin{aligned} &n = 1 :\ \ddot{s} = 0\,, \\ &n = 2 :\ s^{(4)} - 6k\ddot{s}\dot{s}^2 = 0\,, \\ &n = 3 :\ s^{(6)} - 15k^2(\dot{s}^2 s^{(4)} + 4\dot{s}\,\ddot{s}\,\dddot{s} + \ddot{s}^3) + 15k^4\dot{s}^4\ddot{s} = 0, \end{aligned} \tag{70}$$

subject to the boundary conditions

$$\begin{aligned} &n = 1 :\ s(0) = 0; \quad s(T) = S\,, \\ &n = 2 :\ s(0) = \dot{s}(0) = 0; \quad s(T) = S, \quad \dot{s}(T) = 0, \\ &n = 3 :\ s(0) = \dot{s}(0) = \ddot{s}(0) = 0\,; \\ &\qquad s(T) = S, \quad \dot{s}(T) = \ddot{s}(T) = 0\,. \end{aligned} \tag{71}$$

Note that these ODEs (70) are the Euler-Lagrange equations associated with the one-parameter family of cost functionals (60) when inserting the Eqs. (66)–(68) and using the result (69). Interestingly, the Riemannian and Euclidean formulation lead to different movement predictions on the sphere: Whereas both models predict great circles [Fig. 3(a)], the predictions for the speed profiles differ for $n > 1$. These findings can thus serve as a test to which extent a Riemannian or an Euclidean description is more suitable. Unfortunately, the difference in speed profiles on a sphere, as shown in Fig. 3(b), may be too small to be detected experimentally. However, the effect is genuine and may be measurable for point-to-point movements along more general second-order surfaces. Finally, due to the symmetry of the sphere, the coordinate system may be oriented such that along great circles only one coordinate varies (ϑ). The equations (70) can thus be further simplified without loss of generality by inserting $\dot{s} = R\dot{\vartheta}$.

Several experimental studies have been performed to measure hand movements on a spherical surface. The results are not completely conclusive: Whereas Liebermann and colleagues [38] found that geodesics were seldom followed, Sha and co-workers [39] observed an increasing similarity to geodesic paths with practice. It is important to note that different experimental protocols were used in the two studies, and none of them recorded the whole arm configuration during the movement (see remarks in *Case 2*). Speed profiles along the hand paths were in both studies similar to those predicted by Eq. (59), indicating that a Riemannian model formulation provides a better fit to the actual movement data.

Case 2: $\alpha \neq const$. The full metric (56) needs to be taken into account for boundary conditions where the swivel angles at the beginning and the end of the movement are different. Figure 4(a) shows several movement paths on the sphere to a final target location with different final arm postures (different swivel angles). Note that only for $\alpha = const$ the end-effector path is described by a great circle, which might account for the different experimental findings.

Figure 4(c) shows the variation of the swivel angle for these movement paths. Changes of the swivel angle occur more towards the end of the movement where the radial elbow distance r is small. The latter movement strategy results in an overall shorter path as measured by the line element (56).

D. Constrained arm movements along curves with strictly positive curvature

A modified form of the line element (32) can also be applied to movement tasks, where the end effector is constrained to a predefined curve. If the curve can be parametrized by an angle θ, i.e., $\boldsymbol{x} = \boldsymbol{x}(\theta)$, the Euclidean distance becomes $ds^2 = \xi^2 d\theta^2$ with $\xi = \frac{ds}{d\theta}$, and the line element (32) transforms to

$$d\sigma^2 = \xi^2 d\theta^2 + \kappa r^2 d\alpha^2\,. \tag{72}$$

It is well known that tracing movements are described by the empirical one-third power law that relates the hand speed to the curvature of the path [40]. However, the line element (72) does not yet encompass the one-third power law and I will investigate next whether the metric can be adapted accordingly.

Before proceeding, the one-third power law is briefly recapitulated for the readers' convenience. According to this law the periodic tracing of a closed contour with curvature k

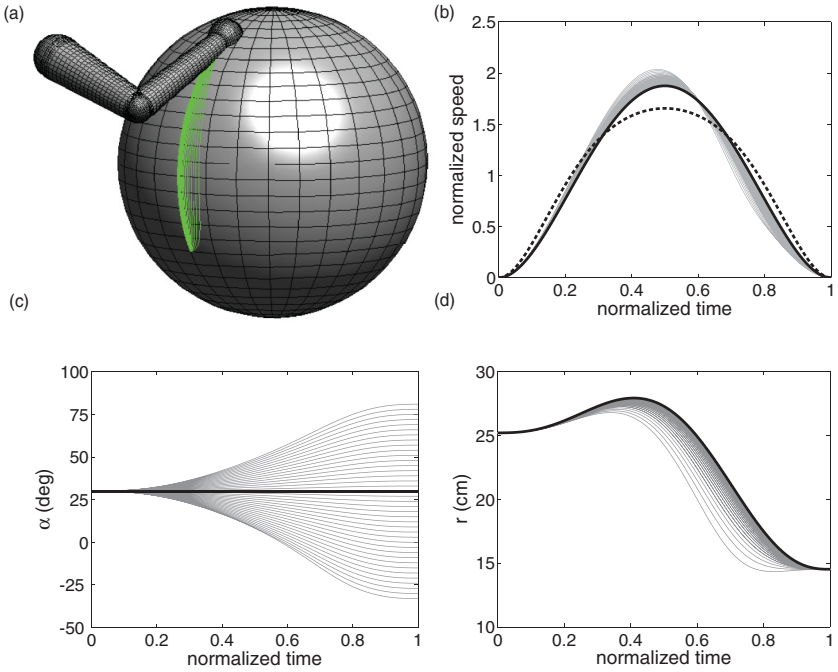

FIG. 4. (Color online) Predictions of the geodesic model with task space metric (56) for movements between pointlike targets on a sphere. (a) Predictions of hand paths. Note that the great circle path is obtained for constant swivel angle. (b) Normalized speed profiles (gray), $\tilde{v} = v/(S/T)$, for movements along the hand paths shown in (a). The solid line shows the speed profile along the great circle path. The dashed line is the speed profile predicted by the classical MJ model when constrained to the sphere. (c) Swivel angle trajectories. (d) Radial distance to the elbow location from the shoulder-hand axis. Simulation parameters are provided in Table I.

results in a hand speed given by

$$v = gk^{-\beta}\,, \tag{73}$$

where g is the constant gain factor and $\beta \approx 1/3$. Assuming that the contour can be parametrized by an angle θ, the gain factor g follows with $v = \xi\dot{\theta}$ from the relation

$$gdt = k^{\beta}\xi d\theta\,, \tag{74}$$

leading to

$$g = \frac{1}{T}\int_0^{2\pi} k^{\beta}\xi d\theta\,, \tag{75}$$

where T is the period of the movement. The one-third power law can thus be written in closed form as

$$v(\theta) = \left(\frac{1}{T}\int_0^{2\pi} k^{\beta}(\theta')\xi(\theta')d\theta'\right)k^{-\beta}(\theta)\,. \tag{76}$$

For a planar elliptic path parametrized by $\boldsymbol{x}(\phi) = [a\cos\phi, b\sin\phi]$, where a and b are the major and minor semiaxes, respectively, one obtains $\xi = \sqrt{a^2\sin\phi^2 + b^2\cos\phi^2}$, $k = ab\xi^{-3}$, and $g = 2\pi(ab)^{1/3}/T$. Thus the hand speed along the elliptic contour according to the one-third power law is

$$v(\phi) = \frac{2\pi}{T}\sqrt{a^2\sin\phi^2 + b^2\cos\phi^2}\,. \tag{77}$$

If instead a polar coordinate representation of the ellipse is used with $\boldsymbol{x}(\theta) = [r_p(\theta)\cos\theta, r_p(\theta)\sin\theta]$ and $r_p(\theta) = ab/\sqrt{b^2\cos^2\theta + a^2\sin^2\theta}$ [the polar radius is denoted here as r_p to distinguish it from the function r defined in (33)] one finds

$$v(\theta) = \frac{2\pi}{T}\sqrt{\frac{b^4\cos^2\theta + a^4\sin^2\theta}{b^2\cos^2\theta + a^2\sin^2\theta}}. \tag{78}$$

Note that the two angles are related by $\theta = \arctan(\frac{b}{a}\tan\phi)$.

The one-third power law can be incorporated into the metric (72) by inserting a conformal factor $\Omega^2(\theta) = [k^{\beta}(\theta)]^2 > 0$, leading to

$$d\sigma^2 = k^{2\beta}(\theta)\xi^2(\theta)d\theta^2 + \kappa r^2(\theta)d\alpha^2\,. \tag{79}$$

It is assumed in the following that the contour has strictly positive curvature ($k > 0$). This restriction will be later removed and a generalization to contours with arbitrary values of k will be given. Note further that the metric (79) does not depend on the swivel angle α and thus adopts the Killing vector field

$$\boldsymbol{\xi} = \frac{\partial}{\partial\alpha}\,. \tag{80}$$

The geodesic equation derived from the line element (79) is

$$\theta'' + \left[\frac{\partial}{\partial\theta}\log\left(k^{\beta}(\theta)\xi(\theta)\right)\right]\theta'^2 - \left[\frac{\kappa}{2[k^{\beta}(\theta)\xi(\theta)]^2}\frac{\partial}{\partial\theta}r^2(\theta)\right]\alpha'^2 = 0\,, \tag{81}$$

$$\alpha'' + \left[\frac{\partial}{\partial\theta}\log r(\theta)\right]\alpha'\theta' = 0\,, \tag{82}$$

where θ and α are functions of an affine path parameter $\lambda \in [0,1]$ and a prime denotes differentiation with respect to λ. The affine parameter λ can be replaced by the normalized arc length $\tilde{\sigma} = \sigma/\Sigma$.

I will show next that the one-third power law is an outcome of the geodesic model with modified metric (79). For this purpose I consider the case of constant and varying swivel angle α separately.

Case 1: $\alpha = const$. The line element (79) for constant swivel angle reduces to

$$d\sigma^2 = k^{2\beta}\xi^2 d\theta^2\,. \tag{83}$$

From (83) one derives

$$\dot{\sigma} = k^{\beta}\xi\dot{\theta}\,, \tag{84}$$

which leads with $v = \xi\dot{\theta}$ to the speed-curvature relation

$$v = \dot{\sigma}k^{-\beta}. \tag{85}$$

A comparison with (73) shows that the gain factor g is given in the Riemannian formulation by the time derivative of the Riemannian arc length. The latter adopts different forms depending on the type of boundary condition imposed.

Periodic movements. The one-third power law (73) follows from (85) for

$$\dot{\sigma} = g = const\,. \tag{86}$$

It remains to be shown that within the framework of the geodesic model $\dot{\sigma}$ is indeed a constant. For periodic tracing movements of closed contours (e.g., an ellipse) with periodic boundary conditions (16), Eq. (17) leads to

$$\dot{\sigma} = \Sigma/T = const\,, \tag{87}$$

and thus the g factor is given by the constant $g = \Sigma/T$, which defines an average "speed" with respect to Riemannian arc length. The form (76) of the one-third power law can be obtained by noting that the total arc length Σ of the contour is

$$\Sigma = \int_0^{2\pi} k^{\beta}(\theta')\xi(\theta')d\theta', \tag{88}$$

and combining Eq. (85) with Eqs. (87) and (88). Note further that (87) can be written as $\frac{d\tilde{\sigma}}{d\tau} = 1$, and thus, arc length is up to a constant time shift a direct measure of time. It is shown next that the one-third power law satisfies the geodesic equation, which reads for $\alpha = \text{const}$:

$$\theta'' + \left[\frac{\partial}{\partial\theta}\log\left(k^{\beta}(\theta)\xi(\theta)\right)\right]\theta'^2 = 0\,. \tag{89}$$

First, for periodic movements normalized arc length in (89) can be replaced by normalized time (reparametrization). Second, the one-third power law (73) leads to $\dot{\theta} = g(k^{\beta}\xi)^{-1}$ and $\ddot{\theta} = -g^2(k^{\beta}\xi)^{-3}\frac{d}{d\theta}(k^{\beta}\xi)$, which satisfy the geodesic equation (89) identically. For example, in the case of an elliptical contour (represented in the ϕ parametrization) the square bracket in (89) vanishes and the solution of the geodesic equation is $\phi = 2\pi\tau$, which leads with $v = \xi\dot{\phi}$ to the result (77). The one-third power law is thus compatible with the geodesic model when applied to the metric space defined by (83).

Discrete movements. I will investigate next tracing movements along contours which are not necessarily closed and which are traced with zero initial and final velocity. Such boundary conditions cannot be analyzed within the original formulation of the one-third power law without further modifications. In the framework of the geodesic model, however, nonperiodic tracing movements can be modeled by imposing two-point boundary conditions of the form (11) leading to

$$\dot{\sigma} = p_n(4\tau(1-\tau))^{n-1}, \tag{90}$$

with peak value $p_n = \frac{\Sigma}{T}\frac{1}{4^{n-1}}\frac{(2n-1)!}{(n-1)!^2}$. The speed-curvature relation (85) then takes the general form

$$v(\theta) = p_n(4\tau(\theta)[1-\tau(\theta)])^{n-1}k^{-\beta}(\theta)\,, \tag{91}$$

where the expression for $\tau(\theta)$ follows from the geodesic model through a sequence of parameter transformations, as I will show next for the special case of $n = 3$. First, from (13) one derives $\tilde{\sigma}(\tau) = (6\tau^5 - 15\tau^4 + 10\tau^3)$ with normalized arc length $\tilde{\sigma} = \sigma/\Sigma$. Second, the inverse of the latter function can be approximated by

$$\tau(\tilde{\sigma}) \approx B(\tilde{\sigma};1-\delta,1-\delta)/B(1;1-\delta,1-\delta)\,, \tag{92}$$

where B is the incomplete β function given by

$$B(z;a,b) = \int_0^z u^{a-1}(1-u)^{b-1}du, \tag{93}$$

and $\delta = 0.641$ is a numerically determined fitting parameter. Finally, the arc length $\tilde{\sigma}$ needs to be expressed in terms of the angle θ. This relation depends on the specific form of the contour and remains to be determined. Thus the speed-curvature relation for $n = 3$ is

$$v(\theta) = \frac{15}{8}\frac{\Sigma}{T}[4\tau(\theta)(1-\tau(\theta))]^2k(\theta)^{-\beta} \tag{94}$$

with

$$\tau(\theta) \approx B(\tilde{\sigma}(\theta);1-\delta,1-\delta)/B(1;1-\delta,1-\delta)\,, \tag{95}$$

where Σ is the arc length of the segment and T denotes the total time needed to trace the segment. If the contour is closed with total arc length $\Sigma_\circ$ and traced once with total tracing time $T_\circ$, Eq. (94) can be rewritten as

$$v(\theta) = \tfrac{15}{8}[4\tau(\theta)(1-\tau(\theta))]^2v_\circ(\theta)\,, \tag{96}$$

where $v_\circ(\theta) = \frac{\Sigma_\circ}{T_\circ}k(\theta)^{-\beta}$ is the speed profile of the periodic movement. It follows that the speed-curvature relation (96) with (95) is given by the one-third power law modulated by a MJ bell-shaped speed profile.

The yet-undetermined contour-specific function $\tilde{\sigma}(\theta)$ will be derived next for an ellipse, cloverleaf, and limaçon (Fig. 5), which are represented in polar coordinates by

$$r_p(\theta) = \begin{cases} \frac{ab}{\sqrt{b^2\cos^2\theta + a^2\sin^2\theta}}\,, & \text{ellipse} \\ a\sin 2\theta, & \text{cloverleaf} \\ a\left(\frac{1}{2}+\cos\theta\right), & \text{limaçon.} \end{cases} \tag{97}$$

Integration of (83) leads to

$$\tilde{\sigma}(\theta) = \begin{cases} \frac{\int_0^{\theta}(b^2\cos^2u + a^2\sin^2u)^{-1}du}{\int_0^{2\pi}(b^2\cos^2u + a^2\sin^2u)^{-1}du}\,, & \text{ellipse} \\ \frac{\int_0^{\theta}(13+3\cos 4u)^{\beta}du}{\int_0^{2\pi}(13+3\cos 4u)^{\beta}du}\,, & \text{cloverleaf} \\ \frac{\int_0^{\theta}(3+2\cos u)^{\beta}du}{\int_0^{2\pi}(3+2\cos u)^{\beta}du}\,, & \text{limaçon.} \end{cases} \tag{98}$$

(If one uses the ϕ parametrization for the ellipse one finds $\tilde{\sigma}(\phi) = \phi/2\pi$.) Figures 5(a)–5(c) show the speed profiles along the three contours for periodic and nonperiodic boundary conditions.

Case 2: $\alpha \neq const$. The case of a varying swivel angle α is relevant for discrete movements where the arm posture is different at the beginning and the end of the movement. The geodesic path is then described by the set of equations (81) and (82). The speed-curvature relation can be derived from the line element (79) leading to

$$v = \sqrt{\dot{\sigma}^2 - \kappa r^2\dot{\alpha}^2}\,k^{-\beta}\,. \tag{99}$$

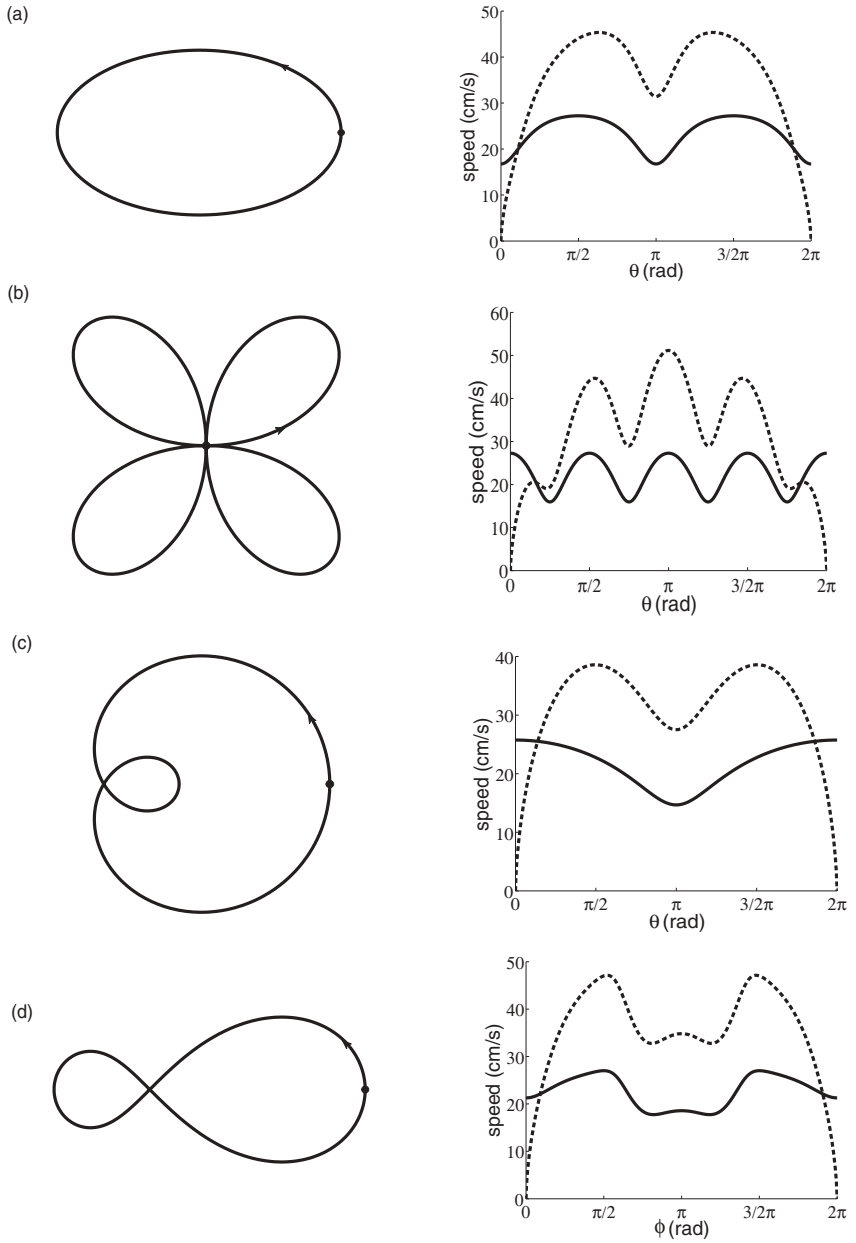

FIG. 5. Predictions of speed profiles resulting from the geodesic model for periodic (solid) and nonperiodic (dashed) tracing movements of an ellipse (a), cloverleaf (b), limaçon (c), and asymmetric lemniscate (d). In the case of nonperiodic boundary conditions the contours were traced once with zero initial and final velocity. All contours have the same perimeter. Note that for the lemniscate contour the generalized speed-curvature relations, (102) and (103), are used. The dot denotes the zero angle position and the arrow indicates the direction of increasing angle. Simulation parameters are provided in Table I.

Thus rotational movements of the elbow lead to an additional modification of the hand-speed profile. Note that for constant swivel angle α the result (85) is recovered.

E. Constrained arm movements along curves with arbitrary curvature

The one-third power law in the form (73) has a singularity at $k = 0$ and is only applicable to contours with strictly positive curvature. In this final section a generalization to smooth contours with arbitrary values of curvature is given by modifying the line element from (83) to

$$d\sigma^2 = (k^2 + \mu^2)^\beta \xi^2 d\theta^2 , \tag{100}$$

where μ is a constant that needs to be adjusted empirically. This leads to a speed-curvature relation of the form

$$v = \dot{\sigma}(k^2 + \mu^2)^{-\beta/2} . \tag{101}$$

Note that the line element results in a speed profile that is symmetric in the curvature k, i.e., $v(k) = v(-k)$, and is regular at $k = 0$. Moreover, for $k > 0$ and $\mu = 0$ the original line element (83) is recovered. As before, the speed-curvature relation (101) transforms for periodic tracing movements to

$$v(\theta) = g[k^2(\theta) + \mu^2]^{-\beta/2}, \tag{102}$$

with $g = \Sigma/T$, whereas for nonperiodic tracing movements one obtains ($n = 3$)

$$v(\theta) = \frac{15}{8}\frac{\Sigma}{T}[4\tau(\theta)(1 - \tau(\theta))]^2[k^2(\theta) + \mu^2]^{-\beta/2}, \tag{103}$$

where $\tau(\theta)$ is given as before by (95). A comparison of the speed-curvature relations given by Eq. (73) and Eq. (102) is provided in Fig. 6. The results derived in this section are applied next to an asymmetric lemniscate contour ("figure of

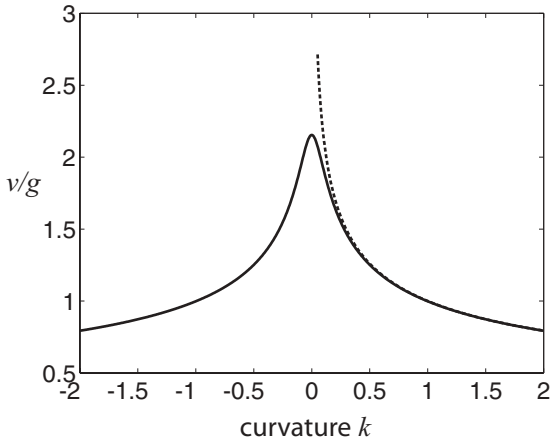

FIG. 6. Comparison of the original one-third power law (dashed), $v/g = k^{-1/3}$, with the modified power law (solid), $v/g = (k^2 + \mu^2)^{-1/6}$, for $\mu = 0.1$. The modified power law is a symmetric function in k and has no singularity at $k = 0$.

eight") with parametric representation

$$x(\phi) = \frac{a(\cos\phi + b)\cos\phi}{1 + \sin^2\phi}, \tag{104}$$

$$y(\phi) = \frac{a(\cos\phi + b)\cos\phi\sin\phi}{1 + \sin^2\phi}, \tag{105}$$

and shape parameters a and b [Fig. 5(d)]. The contour-specific function $\tilde{\sigma}(\theta)$ follows from the integration of (100) and is evaluated numerically. The speed profiles for periodic and nonperiodic tracing movements are shown in Fig. 5(d). Finally, if a varying swivel angle α is additionally taken into account, the speed-curvature relation takes the form

$$v = \sqrt{\dot{\sigma}^2 - \kappa r^2 \dot{\alpha}^2}(k^2 + \mu^2)^{-\beta/2}. \tag{106}$$

IV. DISCUSSION

In this paper the arm configuration manifold has been endowed with different metric structures. Novel distance measures were constructed from arm displacements in task space and together with suitable boundary conditions (periodic or nonperiodic) provided the input to the generalized MJ model (geodesic model). The geodesic model has been applied to a large variety of motor tasks ranging from unconstrained movements between pointlike targets to constrained movements where the end effector was confined to a surface or curve. For all these tasks the spatial movement properties were derived from geodesic paths with respect to the underlying Riemannian manifold and movement timing resulted from a reparametrization of Riemannian arc length into time. For periodic tracing movements along given contours, speed-curvature relations have been analyzed and the compatibility with the empirical one-third power law has been shown. Interestingly, the geometric approach led to a generalization of the one-third power law to nonperiodic boundary conditions and provided a new interpretation of the gain factor as a time derivative of the Riemannian arc length. In addition, movement invariants have been derived from Killing vector fields, which describe the symmetries of the metric tensor. Finally, movement variability can, in principle, be assessed independently of the choice of coordinates in a Riemannian space. These features and examples show that the preshaping of arm configuration space by metric structures in combination with the geodesic model lead to a unique, coordinate-independent modeling framework for human arm movements.

The methods presented in this paper may be used to generate different motor behavior by designing suitable metric structures in the arm configuration manifold and thus, may find applications in robotics and rehabilitation research. One may ask whether similar mechanisms may underlie the control of human arm movements. More precisely, can arm configuration space be shaped by sensorimotor feedback, similar to the preshaping of space presented in this paper, and are geodesics an emergent property of the motor system? A recent study by Danziger and Mussa-Ivaldi [41] seems to answer these questions in the affirmative. The authors studied a highly redundant motor task, where subjects had to control a computer-generated kinematic linkage of two DOFs by continuous finger motion. Depending on the type of visual feedback (entire linkage vs end effector only) the subjects followed different movement strategies. Subjects who received the entire visual feedback followed geodesic paths on a torus, i.e., the configuration manifold of the two-link system. The metric tensor is then given by the (non-Euclidean) pullback metric due to the embedding of the torus into Euclidean space. These findings seem to support the assumption "that the nervous system, through practice, is capable to capture this geometrical structure based on the information contained in the visual feedback" [41]. However, many open questions remain. Does every motor task induce a different metric structure on the arm configuration manifold? How is the geometrical information extracted from the sensorimotor input stream and how is it ultimately encoded by the brain? Are there principles from which the metric tensor for different motor tasks can be derived? It is hoped that future studies with particular emphasis on the geometrical aspects underlying human motor behavior will provide some of the answers.

ACKNOWLEDGMENTS

The author was supported by the German Federal Ministry of Education and Research (BMBF) via the Bernstein Center for Computational Neuroscience (BCCN) Göttingen under Grant No. 01GQ1005B. The author thanks F. Müller-Hoissen for helpful discussions.

APPENDIX A: FORWARD AND INVERSE KINEMATICS

The human arm is modeled as a chain of rigid links. For the description of an arm configuration in terms of four joint angles a parametrization as in [22] is chosen. In this representation the elbow joint location $\boldsymbol{p} = (u,v,w)^T$ and the center of mass of the hand location $\boldsymbol{x} = (x,y,z)^T$ are determined by the joint angles $\boldsymbol{q} = (\theta,\eta,\zeta,\phi)^T$ according to

$$u = -l_1 \sin\theta \sin\eta, \tag{A1}$$

$$v = \; l_1 \sin\theta \cos\eta, \tag{A2}$$

$$w = -l_1 \cos\theta, \tag{A3}$$

$$x = u - l_2[(\cos\theta \sin\eta \cos\zeta + \cos\eta \sin\zeta)\sin\phi + \sin\theta \sin\eta \cos\phi], \quad \text{(A4)}$$

$$y = v + l_2[(\cos\theta \cos\eta \cos\zeta - \sin\eta \sin\zeta)\sin\phi + \sin\theta \cos\eta \cos\phi], \quad \text{(A5)}$$

$$z = w + l_2[\sin\theta \cos\zeta \sin\phi - \cos\theta \cos\phi], \quad \text{(A6)}$$

where l_1 and l_2 are the upper and forearm lengths, respectively. In all derivations it is assumed that $|\boldsymbol{p} \times \boldsymbol{x}| \neq 0$ and $|w| < l_1$.

Another set of four generalized coordinates is defined by $\boldsymbol{q}' = (x,y,z,\alpha)^T$, which consists of the hand coordinates $\boldsymbol{x}$ and the angle α that describes the rotation of the plane spanned by the upper and forearm around the shoulder-hand axis. The rotation angle α is determined by the joint angles according to

$$\tan\alpha = \frac{l_1 \sin\theta \cos\zeta + l_2(\sin\theta \cos\zeta \cos\phi + \cos\theta \sin\phi)}{d \sin\theta \sin\zeta}, \quad \text{(A7)}$$

where $d = |\boldsymbol{x}|$ is the shoulder-hand distance. To derive the functional dependence of the joint angles $\boldsymbol{q}$ on the coordinates $\boldsymbol{q}'$ (inverse kinematics), the joint angles are first expressed by the elbow and hand location. One finds

$$\theta = \operatorname{acos}\left(\frac{-w}{l_1}\right), \quad \text{(A8)}$$

$$\eta = \operatorname{atan2}(-u,v), \quad \text{(A9)}$$

$$\zeta = \operatorname{atan2}(l_1(uy - vx), v(vz - wy) - u(wx - uz)), \quad \text{(A10)}$$

$$\phi = \operatorname{acos}\left(\frac{x^2 + y^2 + z^2 - l_1^2 - l_2^2}{2l_1 l_2}\right), \quad \text{(A11)}$$

where the two argument atan2-function is $\operatorname{atan2}(a,b) := \operatorname{atan}(\frac{a}{b}) - \operatorname{sign}(a)[1 - \operatorname{sign}(b)]\frac{\pi}{2}$. The inverse kinematic relations follow by combining the equations (A8)–(A11) with the relation that expresses the elbow location as a function of hand position and rotation angle α. All elbow positions lie on the intersection circle of two spheres that have centers at the shoulder and hand position with radii l_1 and l_2, respectively. One finds

$$\boldsymbol{p}(\boldsymbol{x},\alpha) = R_z(\varphi)R_y(\vartheta)[f\boldsymbol{e}_x + r\boldsymbol{e}_r(\alpha)], \quad \text{(A12)}$$

where the radial distance to the center of the intersection circle is $f = \frac{1}{2d}(l_1^2 - l_2^2 + d^2)$ and the intersection circle radius is $r = \frac{1}{2d}\sqrt{4d^2 l_1^2 - (l_1^2 - l_2^2 + d^2)^2}$. Furthermore, it is $\varphi = \operatorname{atan2}(y,x)$, $\vartheta = \operatorname{asin}(z/d)$, $\boldsymbol{e}_x = (1,0,0)^T$, $\boldsymbol{e}_r(\alpha) = (0, -\cos\alpha, -\sin\alpha)^T$. R_y and R_z define rotation matrices around the y and z axis, respectively, and are given by

$$R_y(\vartheta) = \begin{pmatrix} \cos\vartheta & 0 & -\sin\vartheta \\ 0 & 1 & 0 \\ \sin\vartheta & 0 & \cos\vartheta \end{pmatrix} \quad \text{(A13)}$$

and

$$R_z(\varphi) = \begin{pmatrix} \cos\varphi & -\sin\varphi & 0 \\ \sin\varphi & \cos\varphi & 0 \\ 0 & 0 & 1 \end{pmatrix}. \quad \text{(A14)}$$

APPENDIX B: PERIODIC BOUNDARY CONDITIONS

In this Appendix the solution of the equation (10) subject to the periodic boundary conditions (71) is derived. For the determination of the temporal aspects it is sufficient to analyze the functional

$$C_n = \int_0^T \left[\frac{d^n\sigma(t)}{dt^n}\right]^2 dt = \frac{1}{T^{2n-1}} \int_0^1 \left[\frac{d^n\sigma(\tau)}{d\tau^n}\right]^2 d\tau, \quad \text{(B1)}$$

where $\tau = t/T$ and T is the period of the movement. The function $\sigma(\tau)$ is periodic in the first and all higher derivatives. A Fourier series "ansatz" for the first derivative leads to

$$\frac{d\sigma(\tau)}{d\tau} = \frac{a_0}{2} + \sum_{k=1}^{\infty} a_k \cos(2\pi k\tau) + b_k \sin(2\pi k\tau). \quad \text{(B2)}$$

Integration of (B2) with boundary conditions (16) results in

$$\sigma(\tau) = \Sigma\tau + \sum_{k=1}^{\infty} \frac{a_k}{2\pi k} \sin(2\pi k\tau) + \frac{b_k}{2\pi k}(1 - \cos(2\pi k\tau)). \quad \text{(B3)}$$

Inserting the expression (B3) into the functional (B1) and performing the integration gives

$$C_n = \frac{1}{T^{2n-1}} \int_0^1 \left[\frac{d^n\sigma(\tau)}{d\tau^n}\right]^2 d\tau = \frac{1}{T^{2n-1}} \left(\sum_{k=1}^{\infty} \frac{1}{2}(2\pi k)^{2n-2}\left(a_k^2 + b_k^2\right) + \delta_{n1}\Sigma^2\right), \quad \text{(B4)}$$

where δ_{nm} is the Kronecker delta. The minimum of the functional for all n is attained for $a_k = b_k = 0, (k = 1,2,\ldots)$, and thus (B3) leads to the solution $\sigma(\tau) = \Sigma\tau$.

APPENDIX C: CENTER OF MASS OF A CYLINDRICAL ARM MODEL

In this derivation a simplified model of the arm is considered, where the upper and forearm are approximated by cylindrical shapes of length l_1 and l_2, respectively, and constant mass density ρ. The center of mass of the arm system is defined by

$$\boldsymbol{x}_{\mathrm{CM}} = \frac{\int_V \boldsymbol{x}\,dm}{\int_V dm} = \frac{\rho \int_V \boldsymbol{x}\,dV}{m_1 + m_2} = \frac{\rho}{m_1 + m_2}\left(\int_{V_1} \boldsymbol{x}\,dV + \int_{V_2} \boldsymbol{x}\,dV\right), \quad \text{(C1)}$$

where m_1, m_2 and V_1, V_2 are the masses and volumes of the upper and forearm, respectively. Let A denote the cross-sectional area of the limbs and $\boldsymbol{e}_1$, $\boldsymbol{e}_2$ the unit vectors in the direction of the upper arm and forearm axes, respectively, then

$$\boldsymbol{e}_1 = \frac{\boldsymbol{p}}{l_1}, \quad \boldsymbol{e}_2 = \frac{\boldsymbol{w} - \boldsymbol{p}}{l_2}, \quad \text{(C2)}$$

where $\boldsymbol{p}$ and $\boldsymbol{w}$ denote the elbow and end-effector locations, respectively. The integrals in (C1) can then be

evaluated as

$$\int_{V_1} \boldsymbol{x} dV = \int_{V_1} r\boldsymbol{e}_1 dV = \int_0^{l_1} r\boldsymbol{e}_1 A dr = \frac{1}{2} l_1^2 A \boldsymbol{e}_1 = \frac{1}{2} V_1 l_1 \boldsymbol{e}_1 , \tag{C3}$$

$$\int_{V_2} \boldsymbol{x} dV = \int_{V_2} (l_1 \boldsymbol{e}_1 + q\boldsymbol{e}_2) dV = \int_0^{l_2} (l_1 \boldsymbol{e}_1 + q\boldsymbol{e}_2) A dq = \left(l_1 l_2 \boldsymbol{e}_1 + \frac{1}{2} l_2^2 \boldsymbol{e}_2 \right) A = \left(l_1 \boldsymbol{e}_1 + \frac{1}{2} l_2 \boldsymbol{e}_2 \right) V_2 . \tag{C4}$$

Inserting (C3) and (C4) in Eq. (C1) leads to the location of the center of mass in terms of the elbow and wrist location:

$$\boldsymbol{x}_{\text{CM}} = \frac{1}{2(m_1 + m_2)} [(m_1 + m_2)\boldsymbol{p} + m_2 \boldsymbol{w}]. \tag{C5}$$

It follows that the center of mass is located in the plane spanned by the upper arm and forearm.

[1] T. Flash and N. Hogan, J. Neurosci. **5**, 1688 (1985).
[2] Y. Uno, M. Kawato, and R. Suzuki, Biol. Cybern. **61**, 89 (1989).
[3] J. Soechting, C. Buneo, U. Hermann, and M. Flanders, J. Neurosci. **15**, 6271 (1995).
[4] C. Harris and D. Wolpert, Nature (London) **394**, 780 (1998).
[5] E. Todorov and J. Jordan, Nat. Neurosci. **5**, 1226 (2002).
[6] E. Todorov, Nat. Neurosci. **7**, 907 (2004).
[7] J. Smeets and E. Brenner, Motor Control **3**, 237 (1999).
[8] A. Piazzi and A. Visioli, IEEE Trans. Ind. Electron. Control Instrum. **47**, 140 (2000).
[9] M. Mihelj, T. Nef, and R. Riener, Adv. Robotics **21**, 843 (2007).
[10] L. Marchal-Crespo and D. J. Reinkensmeyer, J. Neuroeng. Rehabil. **16**, 6 (2009).
[11] B. Rohrer, S. Fasoli, H. Krebs, R. Hughes, B. Volpe, W. Frontera, J. Stein, and N. Hogan, J. Neurosci. **22**, 8297 (2002).
[12] R. Loureiro, F. Amirabdollahaian, M. Topping, B. Driessen, and W. Harwin, Auton. Robotics **15**, 35 (2003).
[13] E. Mach, *Space and Geometry* (The Open Court Publishing Co., Chicago, IL, 1906).
[14] H. Poincaré, *Science and Hypothesis* (Walter Scott Publishing Company, Ltd., London, 1905).
[15] R. Luneburg, *Mathematical Analysis of Binocular Vision* (Princeton University Press, Princeton, NJ, 1947).
[16] J. Koenderink, A. van Doorn, and J. Lappin, Perception **29**, 69 (2000).
[17] J. Todd, A. Oomes, J. J. Koenderink, and A. Kappers, Psychol. Sci. **12**(3), 191 (2001).
[18] J. Todd and J. Norman, Percept. Psychophys. **65**, 191 (2003).
[19] E. Fasse, N. Hogan, B. Kay, and F. Mussa-Ivaldi, Biol. Cybern. **82**, 69 (2000).
[20] T. Flash and A. Handzel, Biol. Cybern. **96**, 577 (2007).
[21] D. Bennequin, R. Fuchs, A. Berthoz, and T. Flash, PLoS Comput. Biol. **5**, e1000426 (2009).
[22] A. Biess, D. Liebermann, and T. Flash, J. Neurosci. **27**, 13045 (2007).
[23] A. Biess, T. Flash, and D. G. Liebermann, Phys. Rev. E **83**, 031927 (2011).
[24] A. Georgopoulos, J. Kalaska, R. Caminiti, and J. Massey, J. Neurosci. **2**, 1527 (1982).
[25] D. Moran and A. Schwartz, J. Neurophysiol. **82**, 2676 (1999).
[26] D. Moran and A. Schwartz, J. Neurophysiol. **82**, 2693 (1999).
[27] A. Schwartz and D. Moran, J. Neurophysiol. **82**, 2705 (1999).
[28] D. Sternad, S. Park, H. Müller, and N. Hogan, PLoS Comput. Bio. **6**, e1000751 (2010).
[29] J. P. Scholz and G. Schöner, Exp. Brain Res. **126**, 289 (1999).
[30] M. do Carmo, *Riemannian Geometry* (CRC Press, Boca Raton, FL, 1992).
[31] M. Žefran, V. Kumar, and C. Croke, IEEE Trans. Robot. Automat. **14**, 576 (1998).
[32] M. Camarinha and F. Leite, IMA J. Math. Control Inf. **12**, 399 (1995).
[33] H. Popiel, Math. Control Signals Syst. **19**, 235 (2007).
[34] H. Machado, F. S. Leite, and K. Krakowski, J. Dynam. Control Syst. **16**, 121 (2010).
[35] M. Nakahara and A. Hilger, *Geometry, Topology and Physics*, Graduate Student Series in Physics (Adam Hilger Publishing, London, 1990).
[36] M. Richardson and T. Flash, J. Neurosci. **22**, 8201 (2002).
[37] J. Synge, Philos. Trans. R. Soc. London, Ser. A **226**, 31 (1927).
[38] T. Krasovsky, S. Bermann, and D. Liebermann, J. Electromyogr. Kines. **20**, 636 (2010).
[39] D. Sha, J. Patton, and A. Mussa-Ivaldi, IJCSS **7**, 41 (2006).
[40] F. Lacquaniti, C. Terzuolo, and P. Viviani, Acta Psychol. **54**, 115 (1983).
[41] Z. Danziger and F. A. Mussa-Ivaldi, J. Neurosci. **32**, 9859 (2012).